Quantitative multi-pinhole small-animal SPECT: uniform versus non-uniform Chang

attenuation correction

NOTE

Quantitative multi-pinhole small-animal SPECT: uniform versus non-uniform Chang attenuation correction

C Wu[1,2]**, J R de Jong**[1]**, H A Gratama van Andel**[2,3]**, F van der Have**[2,3,4]**,
B Vastenhouw**[2,3,4]**, P Laverman**[5]**, O C Boerman**[5]**, R A J O Dierckx**[1]
and F J Beekman[2,3,4]

[1] Department of Nuclear Medicine and Molecular Imaging, University Medical Center
Groningen, University of Groningen, Groningen, The Netherlands
[2] Rudolf Magnus Institute of Neuroscience, University Medical Center Utrecht, Utrecht,
The Netherlands
[3] MILabs B.V., Utrecht, The Netherlands
[4] Section Radiation, Detection and Medical Imaging, Delft University of Technology, Delft,
The Netherlands
[5] Department of Nuclear Medicine, Radboud University Nijmegen Medical Centre, Nijmegen,
The Netherlands

E-mail: wuc@umcg.nl

Abstract

Attenuation of photon flux on trajectories between the source and pinhole apertures affects the quantitative accuracy of reconstructed single-photon emission computed tomography (SPECT) images. We propose a Chang-based non-uniform attenuation correction (NUA-CT) for small-animal SPECT/CT with focusing pinhole collimation, and compare the quantitative accuracy with uniform Chang correction based on (i) body outlines extracted from x-ray CT (UA-CT) and (ii) on hand drawn body contours on the images obtained with three integrated optical cameras (UA-BC). Measurements in phantoms and rats containing known activities of isotopes were conducted for evaluation. In ^{125}I, ^{201}Tl, ^{99m}Tc and ^{111}In phantom experiments, average relative errors comparing to the gold standards measured in a dose calibrator were reduced to 5.5%, 6.8%, 4.9% and 2.8%, respectively, with NUA-CT. In animal studies, these errors were 2.1%, 3.3%, 2.0% and 2.0%, respectively. Differences in accuracy on average between results of NUA-CT, UA-CT and UA-BC were less than 2.3% in phantom studies and 3.1% in animal studies except for ^{125}I (3.6% and 5.1%, respectively). All methods tested provide reasonable attenuation correction and result in high quantitative accuracy. NUA-CT shows superior

accuracy except for ^{125}I, where other factors may have more impact on the quantitative accuracy than the selected attenuation correction.

S Online supplementary data available from stacks.iop.org/PMB/56/N183/mmedia

(Some figures in this article are in colour only in the electronic version)

1. Introduction

Small-animal single-photon emission computed tomography (SPECT) and SPECT/CT play an increasingly important role in biomedical research (Miao *et al* 2007, de Visser *et al* 2007, Zhang *et al* 2008, Hoang *et al* 2009, Golestani *et al* 2010). Accurate and highly reproducible results can be obtained, often even without attenuation correction. However, with improved quantitative accuracy, new research applications may come in reach, e.g. since more subtle differences in tissue function can be detected, and efficacy of drugs or radiation therapy can be monitored and compared longitudinally.

Previous phantom studies (Hwang *et al* 2008) show that photon attenuation reduces the measured activity concentration in the centre of a rat-sized cylinder containing water by up to 50% when imaging with ^{125}I, and up to 25% with ^{99m}Tc. Simulation studies (Chen *et al* 2009) show that the attenuation can reduce reconstructed tracer concentration by up to approximately 40% for ^{125}I and up to about 20% for ^{99m}Tc and ^{111}In even in mouse-sized phantoms. Therefore, attenuation correction, together with correction for effects such as scatter and camera blurring, is important for obtaining highly quantitative SPECT images.

Effects of attenuation and scatter are much smaller in rodents than in humans. Therefore, practical first-order corrections may be sufficient to achieve accurate quantification. With window-based scatter correction (Ogawa *et al* 1991) and iterative attenuation correction (Gullberg *et al* 1985) based on microCT images, Vanhove *et al* (2009) showed that quantitative errors in mouse studies could be reduced to $-7.9 \pm 10.4\%$. We recently introduced an optical-contour-based modified Chang method (Chang 1978) and obtained accurate results as well (1.7% underestimation on average in a phantom study, and 2.1% error on average in a rat study) (Wu *et al* 2010). This Chang attenuation correction does not require an object-dependent system matrix for reconstruction. However, a method based on images obtained with optical cameras has some methodological drawbacks compared to inherently automated CT-based attenuation: (i) the attenuation maps assume homogeneous attenuation, and (ii) the default 3D body contour model needs to be adjusted to individual animals by the operator. While uniform attenuation correction leads to reasonably accurate results, CT-based non-uniform attenuation correction should at least in theory further improve the accuracy and reproducibility of quantification.

Recently, commercial pre-clinical micro-SPECT/CT systems have been developed facilitating CT-based non-uniform attenuation correction. This note presents a modified non-uniform Chang method for quantitative small-animal SPECT. This method was tested with data acquired on a U-SPECT-II/CT system (MILabs, The Netherlands[6]) for ^{125}I, ^{201}Tl, ^{99m}Tc and ^{111}In.

2. Materials and methods

2.1. U-SPECT-II/CT system

The system comprises three stationary detector arrays with multi-pinhole collimators optimized for differently sized rodents with 75 focused pinholes in each cylindrical collimator.

[6] MILabs U-SPECT-II/CT http://www.milabs.com/imaging-solutions/u-spect-ii-ct/

For scanning large volumes—up to the entire animal—an XYZ stage shifts the animal during acquisition. Volume images are then obtained during iterative image reconstruction using all acquired data from all bed positions. Evaluations show that with ^{99m}Tc and ^{123}I, the spatial resolution can reach 0.35 mm for mice and 0.8 mm for rats. These values are only slightly degraded with other commonly used SPECT isotopes like ^{111}In (van der Have *et al* 2009).

The high throughput CT (SkyScan1178, SkyScan, Belgium[7]) comprises a fast circular cone-beam setup dedicated for low-dose scanning with an air-cooled metallo-ceramic tube (voltage range 20–65 kV) and a 1280×1024 pixel 12 bit CCD-based detector. The scanning volume is 82 mm in diameter, with 82 mm length for a single scan and up to 212 mm length with multiple scans. The voxel size is 83 or 166 μm.

2.2. Data acquisition, image reconstruction and registration

SPECT data were acquired in list mode. Images were reconstructed with the scanning focus method (SFM) (Vastenhouw and Beekman 2007) and compensation for blurring effects and distance-dependent pinhole sensitivity through accurate system modelling (van der Have *et al* 2008). Reconstruction was accelerated by using pixel-based ordered subset expectation maximization (POSEM) (Branderhorst *et al* 2010) with 16 subsets and 6 iterations.

CT images were reconstructed using a modified Feldkamp algorithm with automatic adaptation to the scan geometry. Beam hardening and ring artefacts were corrected, and the voxel numbers were converted into Hounsfield units by using a pre-measured calibration factor (CF).

Registration of CT to SPECT images was fully automated using a pre-calculated transformation matrix.

2.3. SPECT CF for quantification

CFs were obtained by acquiring SPECT images of small sources with known activity and were used for converting the reconstructed voxel values to activity concentrations. Since the various distance-dependent pinhole sensitivities were already modelled in the system matrix and subsequently compensated in the reconstruction process (van der Have *et al* 2008), the CF for each isotope should theoretically be homogeneous throughout all voxels of reconstructions if attenuation and scatter can be neglected. This means that the CF for each isotope is a global scaling factor given by

$$CF = \frac{A}{V \cdot \sum R},$$ (1)

where A is the activity of the source measured in a dose calibrator, $\sum R$ is the summation of all voxel values in the reconstructed SPECT image and V is the volume of a voxel. If A has a unit of MBq, V is expressed in ml and the voxel value R is considered to be dimensionless, then the CF has a unit of MBq ml^{-1}.

2.4. Window-based scatter correction

Scatter is a significant source of error (Hwang *et al* 2008, Chen *et al* 2009). Therefore, attenuation correction without scatter correction can lead to overestimation of activity (Wu *et al* 2010). Since effects of scatter in small animals and pinholes are relatively small

---

[7] SkyScan1178 high-throughput micro-CT http://www.skyscan.be/products/1178.htm

Table 1. Window settings for ^{125}I, ^{201}Tl, ^{99m}Tc and ^{111}In (low- and high-energy photopeak).

Window				^{111}In	
(keV ±%)	^{125}I	^{201}Tl	^{99m}Tc	Low	High
Photopeak	28 ± 40%	72 ± 15%	140 ± 10%	171 ± 10%	245 ± 10%
Background 1	14 ± 14.3%	55 ± 9.3%	112 ± 5%	148 ± 3.4%	215 ± 2.3%
Background 2	42 ± 4.8%	88 ± 5.7%	168 ± 3.5%	194 ± 2.6%	275 ± 1.8%

(van der Have and Beekman 2004, 2006, Hutton *et al* 2011), window-based scatter correction methods (Ogawa *et al* 1991) are assumed to be sufficient for isotopes such as ^{99m}Tc and ^{111}In (Hwang *et al* 2008, Vanhove *et al* 2009, Wu *et al* 2010). When imaging with ^{201}Tl, high-energy photons emitted by contaminants can scatter in the collimators and detectors, leading to a rather flat background under the photopeak in the spectrum (Staelens *et al* 2008). This can also be corrected with window-based methods.

Since U-SPECT-II acquires data in list mode, photopeak and background windows can be set after acquisition. The window settings configured in our experiments are listed in table 1. The resulting scatter estimate projections were scaled according to the ratio of the window widths, and incorporated in the POSEM reconstruction according to the Bowsher method (Bowsher *et al* 1996).

2.5. Attenuation map

Intensities of registered CT images were rescaled in order to provide non-uniform attenuation maps for ^{125}I, ^{201}Tl, ^{99m}Tc and ^{111}In. Attenuation coefficients (μ) were calculated for each voxel using the following scaling (LaCroix *et al* 1994):

$$\mu = \mu_0 \left(\frac{\text{HU}}{1000} + 1 \right),\tag{2}$$

where HU is the image intensity in Hounsfield units of a given voxel and μ_0 is the linear attenuation coefficient associated with water and the energy of the photons used in SPECT. μ_0 was obtained by using the NIST data tables (Chantler 2001).

2.6. Post-reconstruction attenuation correction

The Chang algorithm (Chang 1978) is a practical first-order attenuation correction method, which provides an approximation for obtaining the transmitted fraction (TF) for each voxel in reconstructed images. In this method, the TF along every projection line from a certain voxel is calculated, and the average of all these TFs is treated as the overall TF for that voxel:

$$\text{TF} = \frac{1}{M} \sum_{m=1}^{M} \exp \left(- \int_{L_m} \mu(l)\, \mathrm{d}l \right),\tag{3}$$

where M is the number of projections involved in acquisition for data of a certain voxel, L_m denotes the mth projection path of gamma photons and μ is the attenuation coefficient on that projection line L_m. M was set to 64. For non-uniform attenuation correction, attenuation coefficients were derived from CT images according to (2). After the TF of gamma rays for each voxel was estimated, non-uniform attenuation correction was applied:

$$\text{AC} = \frac{U \cdot \text{CF}}{\text{TF}},\tag{4}$$

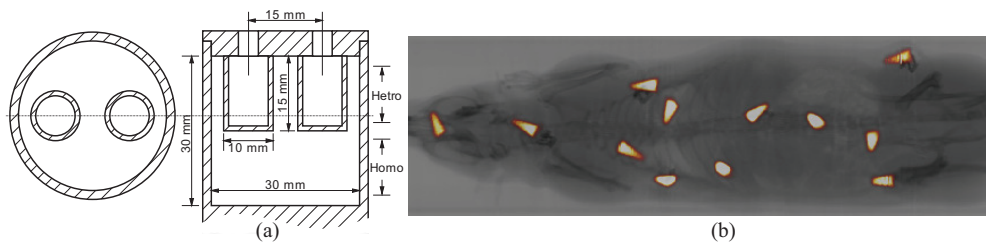with AC the corrected activity concentration and U the voxel value.

Figure 1. (a) Drawing of the NEMA image quality phantom. (b) Rat with artificial sources.

For comparison, two uniform attenuation corrections were performed: (i) based on optical body contours ('UA-BC') (Wu *et al* 2010) and (ii) based on contours extracted from CT using a threshold ('UA-CT'). Non-uniform attenuation correction with the attenuation coefficients derived from the CT data will be hereinafter referred to as 'NUA-CT'.

2.7. Phantom experiments

We used the NEMA image quality phantom for small-animal imaging (NEMA NU 4-2008, figure 1(a)) to validate accuracy of attenuation correction. The phantom consists of a cylindrical fillable chamber (30 mm inside diameter and 30 mm length), and a lid with two empty chambers (10 mm outside diameter and 15 mm length).

The phantom was first filled with $^{99m}TcO_4^-$ solution (8.65 MBq ml^{-1}). The activity was measured in the same dose calibrator that was used for the SPECT calibration. Next, SPECT and fully circular CT (60 kV and 615 μA) were performed. SPECT images were reconstructed with decay and scatter correction. The same procedure was repeated for $^{201}TlCl_3$, $^{111}InCl_3$ and Na^{125}I solution, with activity concentrations of 5.90 MBq ml^{-1}, 5.91 MBq ml^{-1} and 4.54 MBq ml^{-1}, respectively.

2.8. Animal experiments

We used four cadavers of female Wistar rats (300–350 g body weight) to test the method with realistic attenuation distributions. For each isotope, 12 small sources with volumes of around 0.2 ml were made from tips of 0.5 ml microcentrifuge tubes (Eppendorf, Hamburg, Germany), radioactive solution and Parafilm (Pechiney Plastic Packaging Company, Chicago, IL, USA). Activities of ^{125}I, ^{201}Tl, ^{99m}Tc and ^{111}In sources ranged from 8.30 to 11.8 MBq, 3.82 to 7.23 MBq, 13.9 to 18.8 MBq and 6.02 to 11.7 MBq, respectively. The activity in the sources was measured in the same dose calibrator. These sources were inserted into the four rats surgically (inside or nearby mouth, neck, left and right lungs, liver, stomach, left kidney, intestine, left and right shoulders, and left and right sides of waist, as shown in figure 1(b)). Total-body SPECT/CT was performed for each rat.

3. Results

3.1. Phantom experiments

Figure 2 shows 10 mm slices and line profiles of the reconstructed ^{99m}Tc phantom images. Images of other isotopes can be found in the supplementary data available at stacks.iop.org/PMB/56/N183/mmedia (figures S1–S5). Significant differences were found between uncorrected and corrected results, while the contrasts among corrected results with
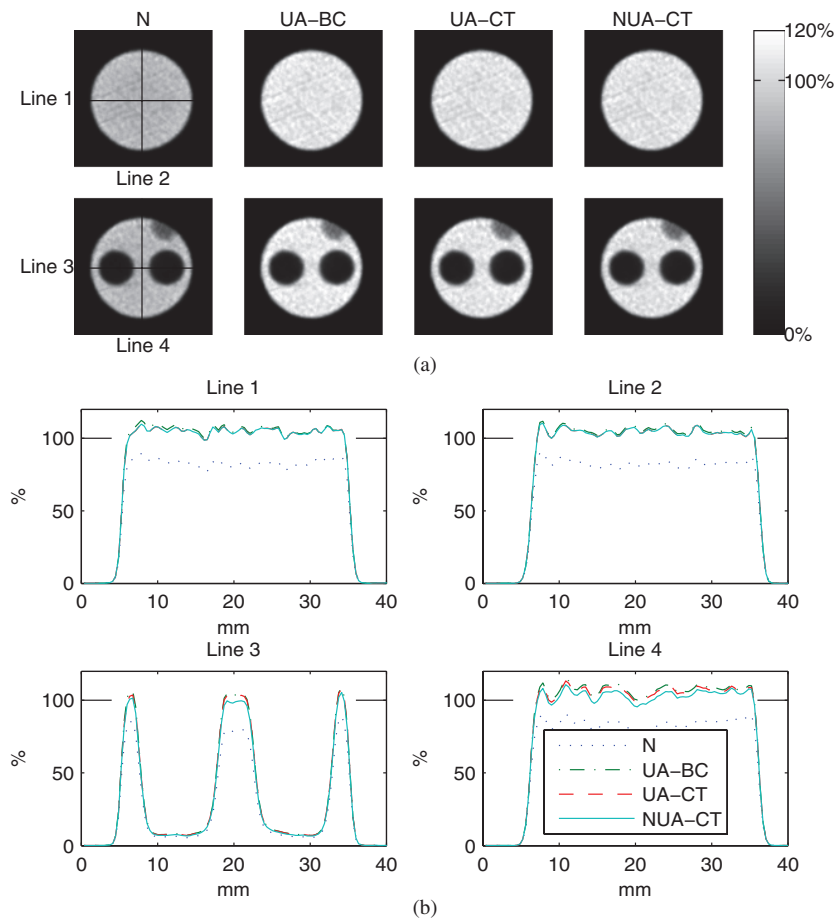
Figure 2. Results of ^{99m}Tc phantom. (a) Slices without attenuation correction (N), with optical-contour-based correction (UA-BC), with CT-contour-based correction (UA-CT) and with CT-image-based correction (NUA-CT). (b) Line profiles through the centre of slices. Note that the gold standard is 100%.

the three different methods were small. The gold standards were activity concentrations measured in a dose calibrator. When UA-BC was used, the deviations from the gold standards were −1.9%, 8.4%, 7.0%, 5.1%, 11.4% and 11.5% for ^{125}I, ^{201}Tl, ^{99m}Tc, ^{111}In (low-energy photopeak), ^{111}In (high-energy photopeak) and ^{111}In (both photopeaks), respectively. These errors were altered to −3.3%, 8.0%, 5.7%, 3.6%, 9.9% and 10.0% with UA-CT, respectively, and to −5.5%, 6.8%, 4.9%, 2.8%, 9.2% and 9.2%, respectively, by using NUA-CT. In contrast, errors of −41.9%, −17.2%, −15.5%, −16.1%, −9.0% and −10.0% were found when no attenuation correction was performed. Besides the overall activity concentrations, we also divided the entire volume into homogeneous and heterogeneous regions (indicated in figure 1(a) as 'Homo' and 'Hetro', respectively) and calculated their activity concentrations separately. These results are listed in table 2.

3.2. Animal experiments

Activities in the regions of interest containing the sources in both uncorrected and corrected images were calculated, and compared with the gold standards measured in the dose calibrator.

Table 2. Quantitative errors of phantom images by using different attenuation correction methods.

Error (in %)	No correction	UA-BC	UA-CT	NUA-CT
^{125}I				
Homogeneous	−42.2	−1.8	−3.2	−4.0
Heterogeneous	−41.5	−2.1	−3.5	−7.9
^{201}Tl				
Homogeneous	−17.7	8.1	7.7	7.3
Heterogeneous	−16.4	8.9	8.6	6.0
^{99m}Tc				
Homogeneous	−16.3	6.0	4.8	4.8
Heterogeneous	−14.0	8.7	7.3	5.1
^{111}In (low)				
Homogeneous	−17.1	4.1	2.5	2.4
Heterogeneous	−14.5	6.7	5.3	3.4
^{111}In (high)				
Homogeneous	−9.6	10.9	9.4	9.3
Heterogeneous	−8.1	12.1	10.7	8.9
^{111}In (both)				
Homogeneous	−10.8	10.8	9.2	9.1
Heterogeneous	−8.6	12.7	11.3	9.4

Results are plotted in figure 3 for each source. For ^{125}I, the relative errors of the activities measured on the image without attenuation correction, with UA-BC, with UA-CT and with NUA-CT, were on average −47.0%, 7.2%, 2.3% and 2.1%, respectively. For ^{201}Tl, these errors were −26.8%, 5.5%, 2.7% and 3.3%. For ^{99m}Tc, the same errors were −24.1%, 2.5%, 2.0% and 2.0%. For ^{111}In (low-energy photopeak), they were −23.4%, 3.2%, 0.1% and 2.0%; for ^{111}In (high-energy photopeak), they were −19.8%, 4.6%, 2.0% and 3.8%; and for ^{111}In (both photopeaks), they were −21.0%, 4.8%, 1.8% and 3.7%, respectively. These values are listed in table 3 together with standard deviations of the relative errors.

4. Discussion

In the present study, a Chang-based non-uniform attenuation correction method was developed and its impact on the accuracy of quantitative analysis of SPECT images was determined. For the standard small-animal NEMA image quality phantom, the underestimation of activity concentration due to photon attenuation ranged from 9.0% to 41.9% for different isotopes when no correction was applied, which was in line with Chen *et al* (2009). With each of the three attenuation correction methods, the relative error reduced to less than 10% except for the ^{111}In high-energy-photopeak and ^{111}In both-photopeak images. There was a trend towards a slight overestimation in images involving the ^{111}In high-energy photopeak. This is because the system matrices were made from scans with ^{99m}Tc. The 245 keV photons emitted by ^{111}In have a higher possibility of penetrating the collimator directly, which is not yet accurately modelled in the system matrices. In this sense, although ^{111}In images are usually reconstructed using both photopeaks to increase the signal-to-noise ratio, especially when the number of counts collected is not high enough, it may be better to use only the low-energy photopeak for quantitative purposes in studies with sufficiently high activity. Future investigations about
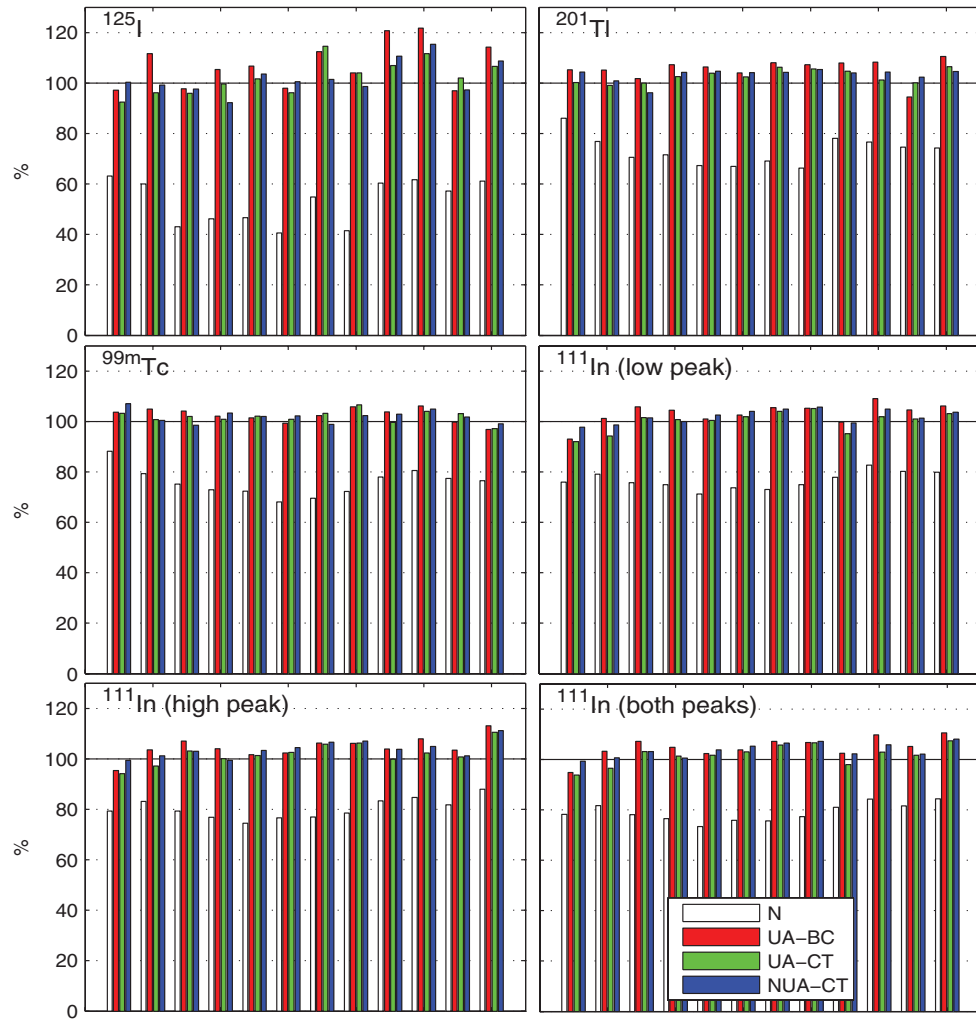
Figure 3. Results of animal studies with different isotopes. N: without attenuation correction, UA-BC: with optical-contour-based correction, UA-CT: with CT-contour-based correction and NUA-CT: with CT-image-based correction. Note that the gold standard is 100%.

optimal window-settings and correction of ^{111}In images at different count levels may lead to further improvement of quantification for ^{111}In imaging.

For ^{125}I, ^{201}Tl, ^{99m}Tc and for the ^{111}In low-energy-photopeak data, differences of the average accuracy after attenuation correction by using UA-BC and UA-CT were between 0.4% and 1.5%. Since these two methods use exactly the same algorithm, the differences in the results can only be explained by the differences of contour extraction. Use of the CT contours led to slightly more accurate results except for [125]I.

When comparing UA-CT and NUA-CT, we can see that in the homogeneous region of the phantom, the two methods lead to similar results (difference < 0.8%). However, in the heterogeneous region, NUA-CT is superior to UA-CT for ^{201}Tl, ^{99m}Tc and ^{111}In low-energy-photopeak images, though differences are small (<2.6%). This could be explained by the uniform and non-uniform TF maps calculated from the different methods. Taking

Table 3. Quantitative errors of rat images by using different attenuation correction methods.

Error (in %)	No correction	UA-BC	UA-CT	NUA-CT
^{125}I				
Average	−47.0	7.2	2.3	2.1
std.	8.8	9.0	6.7	6.5
^{201}Tl				
Average	−26.8	5.5	2.7	3.3
std.	5.7	4.2	2.6	2.5
^{99m}Tc				
Average	−24.1	2.5	2.0	2.0
std.	5.5	2.8	2.4	2.5
^{111}In (low)				
Average	−23.4	3.2	0.1	2.0
std.	3.4	4.1	4.1	2.7
^{111}In (high)				
Average	−19.8	4.6	2.0	3.8
std.	4.0	4.2	4.3	3.4
^{111}In (both)				
Average	−21.0	4.8	1.8	3.7
std.	3.6	4.1	4.1	2.9

the TF maps for ^{99m}Tc as an example (figure S6 in supplementary data available at stacks.iop.org/PMB/56/N183/mmedia), the TFs of about three quarters of the voxels have differences less than 2% between the uniform and non-uniform maps. The largest difference was less than 6.9% and was located in the air-filled chambers. For ^{125}I, because the amount of attenuation is higher than for the other isotopes, the difference in results between using NUA-CT and UA-CT is also higher, about 4.4% on average.

Only the attenuation-corrected ^{125}I images suffered from underestimation. Quantitative accuracy was the best for UA-BC and worst for NUA-CT. This may be caused by errors in scatter correction and reconstruction. The coherent scattering of low-energy photons cannot be simply corrected by using the energy-window-based method. Therefore, part of the activity was wrongly attributed to the air-filled chambers (figure S1(b) in supplementary data available at stacks.iop.org/PMB/56/N183/mmedia), and consequently reconstructed activity in the solution-filled area decreased. In addition, some distortions in the shape of the phantom were observed in the ^{125}I and ^{201}Tl images (figures S1(a) and S2(a) in supplementary data available at stacks.iop.org/PMB/56/N183/mmedia). This can be explained by the fact that the system point spread functions (PSFs) were calibrated with ^{99m}Tc. We expect that more extensive calibration with different isotopes or correction of PSFs for the photon energy (e.g. along the lines in Goorden *et al* (2011)) will further improve the results. However, note that neither of these approaches is trivial to implement.

In rat cadavers, we obtained quantitative errors in un-corrected images which again were in line with experiments of Hwang *et al* (2008). As expected, UA-BC gave the worst (but still quite accurate) estimation of the activities. Comparing with UA-CT that uses more accurate contours, we found that the estimations of attenuation by using UA-BC were higher. This means that the hand-draw contours may have been drawn too loose, which may be caused by the fur of the rats. Surprisingly, UA-CT performed as well as NUA-CT.

The Chang algorithm, either uniform or non-uniform, is a first-order approximation. We expect that the quantitative accuracy would progressively increase by using UA-BC, UA-CT and NUA-CT. This coincides with the phantom-experiment results quite well. However, in the rat studies, the advantage of NUA-CT is not obvious comparing to UA-CT. One reason could be that there are no large structures with higher or lower density than soft tissue in the rat bodies, unlike in the heterogeneous region of the phantom. The volume containing bones is small, and the air content of the lungs was low, since the rats were euthanized before the scans. In studies with living animals, the effect of non-uniform attenuation correction will be somewhat larger. Otherwise, noise and artefacts in CT images may cancel out part of the benefit from non-uniform attenuation correction.

The linear scaling that we have used for translating CT numbers to attenuation coefficients is an approximate approach. However, it has the advantage that no extra CT measurements with dense materials are required. This linear approach seems to be sufficient for accurate attenuation correction in small animals, likely because of the small dimension of bone structure. If any significant improvements can still be made needs to be tested in future experiments.

5. Conclusion

We introduced a CT-image-based first-order Chang method for non-uniform attenuation correction in SPECT with focusing pinholes. Phantom and animal experiments were conducted with different isotopes (i.e. ^{125}I, ^{201}Tl, ^{99m}Tc and ^{111}In). Results were compared with two uniform attenuation correction methods based on contours extracted from optical images or CT images. We conclude that all the three methods allow accurate absolute quantification in small-animal SPECT, while the CT-based methods improve the accuracy as compared to the optical-contour-based one. It is a good choice just to use the optical-contour-based method for small-animal studies in which quantification is needed but no CT scans are available. When CT images are used, the creation of the attenuation maps is slightly more accurate and is automated, which can save time and operator training for drawing the contours.

Acknowledgment

References

Bowsher J E, Johnson V E, Turkington T G, Jaszczak R J, Floyd C E and Coleman R E 1996 Bayesian reconstruction and use of anatomical *a priori* information for emission tomography *IEEE Trans. Med. Imaging* **15** 673–86

Branderhorst W, Vastenhouw B and Beekman F J 2010 Pixel-based subsets for rapid multi-pinhole SPECT reconstruction *Phys. Med. Biol.* **55** 2023–34

Chang L T 1978 A method for attenuation correction in radionuclide computed tomography *IEEE Trans. Nucl. Sci.* **25** 638–43

Chantler C T 2001 Detailed tabulation of atomic form factors, photoelectric absorption and scattering cross section, and mass attenuation coefficients in the vicinity of absorption edges in the soft x-ray ($Z= 30$–36, $Z = 60$–89, $E = 0.1$–10 keV)—addressing convergence issues of earlier work *J. Synchrotron Radiat.* **8** 1124

Chen C L, Wang Y, Lee J J and Tsui B M 2009 Toward quantitative small animal pinhole SPECT: assessment of quantitation accuracy prior to image compensations *Mol. Imaging Biol.* **11** 195–203

de Visser M, Bernard H F, Erion J L, Schmidt M A, Srinivasan A, Waser B, Reubi J C, Krenning E P and de Jong M 2007 Novel ^{111}In-labelled bombesin analogues for molecular imaging of prostate tumours *Eur. J. Nucl. Med. Mol. Imaging* **34** 1228–38

Golestani R, Wu C, Tio R A, Zeebregts C J, Petrov A D, Beekman F J, Dierckx R A, Boersma H H and
Slart R H 2010 Small-animal SPECT and SPECT/CT: application in cardiovascular research *Eur. J. Nucl. Med. Mol. Imaging* **37** 1766–77

Goorden M C, van der Have F, Kreuger R and Beekman F J 2011 An efficient simulator for pinhole imaging of PET isotopes *Phys. Med. Biol.* **56** 1617–34

Gullberg G T, Huesman R H, Malko J A, Pelc N J and Budinger T F 1985 An attenuated projector-backprojector for iterative SPECT reconstruction *Phys. Med. Biol.* **30** 799–816

Hoang B, Lee H, Reilly R M and Allen C 2009 Noninvasive monitoring of the fate of ^{111}In-labeled block copolymer micelles by high resolution and high sensitivity microSPECT/CT imaging *Mol. Pharm.* **6** 581–92

Hutton B F, Buvat I and Beekman F J 2011 Review and current status of SPECT scatter correction *Phys. Med. Biol.* **56** R85–112

Hwang A B, Franc B L, Gullberg G T and Hasegawa B H 2008 Assessment of the sources of error affecting the quantitative accuracy of SPECT imaging in small animals *Phys. Med. Biol.* **53** 2233–52

LaCroix K J, Tsui B M W, Hasegawa B H and Brown J K 1994 Investigation of the use of x-ray CT images for attenuation compensation in SPECT *IEEE Trans. Nucl. Sci.* **41** 2793–9

Miao Y, Benwell K and Quinn T P 2007 ^{99m}Tc- and ^{111}In-labeled alpha-melanocyte-stimulating hormone peptides as imaging probes for primary and pulmonary metastatic melanoma detection *J. Nucl. Med.* **48** 73–80

Ogawa K, Harata Y, Ichihara T, Kubo A and Hashimoto S 1991 A practical method for position-dependent Compton-scatter correction in single photon-emission CT *IEEE Trans. Med. Imaging* **10** 408–12

Staelens S G, de Wit T C, Lemahieu I A and Beekman F J 2008 Degradation of myocardial perfusion SPECT images caused by contaminants in thallous (^{201}Tl) chloride *Eur. J. Nucl. Med. Mol. Imaging* **35** 922–32

van der Have F and Beekman F J 2004 Photon penetration and scatter in micro-pinhole imaging: a Monte Carlo investigation *Phys. Med. Biol.* **49** 1369–86

van der Have F and Beekman F J 2006 Penetration, scatter and sensitivity in channel micro-pinholes for SPECT: a Monte Carlo investigation *IEEE Trans. Nucl. Sci.* **53** 2635–45

van der Have F, Vastenhouw B, Ramakers R M, Branderhorst W, Krah J O, Ji C, Staelens S G and Beekman F J 2009 U-SPECT-II: an ultra-high-resolution device for molecular small-animal Imaging *J. Nucl. Med.* **50** 599–605

van der Have F, Vastenhouw B, Rentmeester M and Beekman F J 2008 System calibration and statistical image reconstruction for ultra-high resolution stationary pinhole SPECT *IEEE Trans. Med. Imaging* **27** 960–71

Vanhove C, Defrise M, Bossuyt A and Lahoutte T 2009 Improved quantification in single-pinhole and multiple-pinhole SPECT using micro-CT information *Eur. J. Nucl. Med. Mol. Imaging* **36** 1049–63

Vastenhouw B and Beekman F 2007 Submillimeter total-body murine imaging with U-SPECT-I *J. Nucl. Med.* **48** 487–93

Wu C, van der Have F, Vastenhouw B, Dierckx R A, Paans A M and Beekman F J 2010 Absolute quantitative total-body small-animal SPECT with focusing pinholes *Eur. J. Nucl. Med. Mol. Imaging* **37** 2127–35

Zhang J, Nie L, Razavian M, Ahmed M, Dobrucki L W, Asadi A, Edwards D S, Azure M, Sinusas A J and Sadeghi M M 2008 Molecular imaging of activated matrix metalloproteinases in vascular remodeling *Circulation* **118** 1953–60